

# Identifying heterogeneous micromechanical properties of biological tissues via physics-informed neural networks

Wensi Wu<sup>1,2</sup>, Mitchell Daneker<sup>3,4</sup>, Kevin T. Turner<sup>5</sup>, Matthew A. Jolley<sup>1,2</sup>, and Lu Lu<sup>3,\*</sup>

<sup>1</sup>Department of Anesthesiology and Critical Care Medicine, Children's Hospital of Philadelphia, Philadelphia, PA 19104

<sup>2</sup>Division of Cardiology, Children's Hospital of Philadelphia, Philadelphia, PA 19104

<sup>3</sup>Department of Statistics and Data Science, Yale University, New Haven, CT 06511

<sup>4</sup>Department of Chemical and Biochemical Engineering, University of Pennsylvania, Philadelphia, PA 19104

<sup>5</sup>Department of Mechanical Engineering and Applied Mechanics, University of Pennsylvania, Philadelphia, PA 19104

\*Corresponding author. Email: lu.lu@yale.edu

## ABSTRACT

The heterogeneous micromechanical properties of biological tissues have profound implications across diverse medical and engineering domains. However, identifying the full-field heterogeneous elastic properties of soft materials using traditional computational and engineering approaches is fundamentally challenging due to difficulties in estimating local stress fields. Recently, there has been a growing interest in using data-driven models to learn full-field mechanical responses such as displacement and strain from experimental or synthetic data. However, research studies on inferring the full-field elastic properties of materials, a more challenging problem, are scarce, particularly for large deformation, hyperelastic materials. Here, we propose a novel approach to identify the elastic modulus distribution in nonlinear, large deformation hyperelastic materials utilizing physics-informed neural networks (PINNs). We evaluate the prediction accuracies and computational efficiency of PINNs, informed by mechanic features and principles, across three synthetic materials with structural complexity that closely resemble real tissue patterns, such as brain tissue and tricuspid valve tissue. Our improved PINN architecture accurately estimates the full-field elastic properties, with relative errors of less than 5% across all examples. This research has significant potential for advancing our understanding of micromechanical behaviors in biological materials, impacting future innovations in engineering and medicine.

## 1 Introduction

Biological tissues exhibit a vast range of structural and mechanical heterogeneity<sup>1,2</sup>. These properties have significant medical implications for both normal physiological function and disease. Research studies have shown that tissue biomechanical properties have a strong correlation to various cardiovascular diseases, including aortic dissection<sup>3</sup>, aortic aneurysm<sup>4-6</sup>, myocardial infarction<sup>7</sup>, and degenerated heart valves<sup>8</sup>. Further, tissue mechanical properties also play a critical role in cancer invasion<sup>9</sup>, tissue regenerative capacity<sup>10-13</sup>, host reaction upon implantation<sup>14-17</sup>, and fibrosis<sup>18,19</sup>. Computational analysis, such as finite element modeling, has advanced our understanding of the physiological processes underlying these medical phenomena. However, despite the significant progress made in this field, many existing models rely on simplified constitutive models due to insufficient methodology to capture the complexities of material properties in soft tissues<sup>20,21</sup>. This, in turn, impedes clinical translation of patient-specific computational analysis to inform medical decision making<sup>22-25</sup>.

The unique combination of soft material microstructure and properties not only provides indicators for diseases but also introduces various beneficial mechanical properties and functionalities that surpass those found in conventional materials. These desirable soft material characteristics have initiated researchers in additive manufacturing, materials science, and mechanics communities to explore the possibilities of biomimetic materials<sup>26,27</sup>, leading to innovative research in the design of artificial organs<sup>28–30</sup>, soft robots<sup>31,32</sup>, and wearable devices<sup>33</sup>. Despite the apparent advantages of heterogeneous material design, including lower manufacturing costs, enhanced product usability, and improved end-user experience, there is a scarcity of investigations into the relationship between heterogeneous material properties and consequent functions, hindering the full realization of the functional potential of biomimetic materials<sup>34</sup>.

Atomic force microscopy (AFM) indentation and tensile test are two popular mechanical testing methods for determining the elastic properties of biological tissues. AFM is particularly effective for examining heterogeneous structures and properties of specimens at the cellular level<sup>35,36</sup>. This method scans the tissue samples and applies perpendicular pressure to measure the resultant deformation at each probe location. Although this approach generates high spatial resolution maps of elastic moduli, the indentation loading conditions are not representative of physiological conditions of living tissues<sup>37,38</sup>, thus lacking relevance for the study of human disease and the mechanical behaviors of biological tissues.

On the other hand, in tensile testing, traction or deformation are applied to the boundaries of tissue samples. Digital image correlation (DIC) is utilized to capture the material deformation. Subsequent inverse finite element analysis and optimization methods are applied to identify the macroscopic constitutive parameters of the material<sup>39–41</sup>. While it is relatively straightforward to approximate stress distribution on the boundary of a testing specimen, extracting internal stress is non-trivial and often relies on a complex multiscale modeling approach<sup>42–44</sup>. Consequently, tensile testing has primarily been confined to the macroscopic homogeneous elastic properties of the material.

Recently, researchers have begun to explore the application of data-driven methods to overcome the limitations mentioned above. In the context of mechanics, researchers have experimented with machine learning frameworks and architectures (*e.g.*, convolutional neural networks, neural operators, and generative adversarial networks) to predict the mechanical responses and identify the elastic property map of heterogeneous materials of synthetical data<sup>45–48</sup>. These methods have achieved high prediction accuracy. However, the drawback of data-driven approaches is that they typically require a large number of datasets, on the order of thousands to millions of image pairs (*i.e.*, an input image representing data to be analyzed and an output image corresponding to the expected outcome), in order for the machine learning model to accurately learn their latent relation. Collecting a sufficient volume of images for successfully implementing a machine-learning model may require an impractical amount of effort and resources.

Physics-informed machine learning<sup>49,50</sup> provides an excellent alternative to traditional data-driven machine learning approaches in situations where the data is scarce<sup>51–53</sup>. Physics-informed neural networks (PINNs) have been utilized to determine the material parameters of homogenous structures within linear elastic, linear dynamic, hyperelastic, nonlinear-elastoplastic, and anisotropic constitutive models<sup>54–56</sup>. This approach has also been extended to identify the material parameters of structures with additional internal inclusions<sup>57–59</sup>. Recently, this has also been applied to linear elastic heterogeneous materials<sup>60,61</sup>. It has been observed that PINNs struggle to converge in the presence of high-frequency functions or highly heterogeneous features<sup>62–64</sup>. As such, researchers have explored the application of Fourier-feature PINNs to simulate seismic wavefields<sup>65</sup>, 1D radiation transport equations in heterogeneous media<sup>66</sup>, and identify parameters in system-biology-informed ordinary differential equations (ODEs) problems<sup>67,68</sup>.

The present research aims to tackle the more complex inverse problem that involves realistic tissue structural patterns and nonlinear material constitutive models. In particular, we aim to investigate the applicability and generality of PINNs for characterizing the nonlinear, hyperelastic properties of biological

tissues such as brain tissue and tricuspid valve tissue, with an emphasis on discovering a high-fidelity map of complex elasticity fields in soft tissues using standard and Fourier-feature PINNs, as well as investigating the relationship between neural network architectures and prediction accuracy. This foundational work will be extensible to accurately estimate *in vivo* tissue properties from medical images and study the evolution of tissue microscopic elastic properties in response to mechanical loadings. We summarize the major contributions and significance of the current work as follows.

- We introduce a novel approach, using state-of-the-art PINN techniques, to discover the elastic modulus distribution in complex heterogeneous hyperelastic materials that have traditionally been challenging and mathematically ill-posed.
- We demonstrated that PINNs have remarkable potential for providing highly accurate parameter estimations using just one data sample. This is a significant breakthrough, as building an accurate machine-learning model through data-driven techniques can be time-consuming and impractical.
- We analyzed the estimation accuracy of 20 neural network architectures, informed by mechanic features and principles, on three computational materials with complex local features. We identified a top-performing neural network architecture that consistently produces accurate estimations of the full-field elastic modulus. Further, the consistent accuracy of our selected top-performing neural network architecture suggests the generality of our method.
- This work provides a promising approach to studying the effect of material heterogeneity in their macroscopic behaviors and the evolution of material micromechanical properties in response to mechanical load. This is highly applicable to studying tissue growth and remodeling<sup>69–71</sup>, detecting early mechanical markers of cancer cell invasion<sup>72</sup>, and developing theoretical insights into the yield behavior of metallic alloys<sup>73,74</sup>.

## 2 Results

Understanding how tissue microstructure relates to its mechanical properties and behaviors is crucial for maintaining tissue health. While some studies have explored how tissue microstructure affects its macroscopic mechanical properties<sup>75–77</sup>, research on the relationship between tissue microstructure and the corresponding elasticity field is limited. This study aims to uncover the elasticity field within soft tissue microstructural components using PINNs.

### 2.1 Problem setup

Fig. 1 illustrates the structural pattern of three heterogeneous tissue specimens considered in the present work. The structural pattern of the first example was constructed using a Gaussian random field (GRF)<sup>78</sup> (Fig. 1A). The second example represents the cell bodies within a brain tissue<sup>79</sup> (Fig. 1B). The third example demonstrates the fibrosis network of the tricuspid valve leaflets<sup>80</sup> (Fig. 1C). We adopted a complexity measure based on image information theory, namely Delentropy<sup>81,82</sup>, to evaluate the complexity of tissue microstructural patterns. Delentropy captures the relative relation between the local and global features by analyzing the gradient vector field of the image. This measure provides a useful metric to evaluate the performance of machine learning models in the context of data complexity.

To generate reference strain data, we first assumed an elastic moduli distribution ( $E$ ) for the tissue microstructure in the image. We then used the elastic distribution to compute the full-field strain data ( $\varepsilon_{xx}$ ,  $\varepsilon_{yy}$  and  $\varepsilon_{xy}$ ) using finite element analysis (FEA). Lastly, we integrated the full-field strain data in PINNs

to guide the discovery of the heterogeneous elastic moduli distribution of the tissue microstructure, cell bodies, and fibrosis network in PINNs.

## 2.2 PINN overview

Fig. 2 provides an overview of the network architectures in the present work. We examined the performance of four variants of PINNs, depicted in Figs. 2A to D. Figs. 2A and B represent standard PINNs architectures with and without enforcing boundary constraints, whereas Figs. 2C and D display Fourier-feature PINNs architectures with and without enforcing boundary constraints. Additionally, we identified five unique fully connected NN (FCNN) architectures (Fig. 2E) to investigate the prediction accuracy of the constitutive elastic properties within each PINNs variant. All simulations were performed on NVIDIA A100-SXM4-40GB GPUs. Detailed information related to Fourier-feature PINNs is described in Section 2.2.2.

### 2.2.1 PINN architectures

In the following, we briefly summarize the five FCNN architectures (Fig. 2E). We denote the output variables of FCNN I and FCNN II by  $N_{u_i^*}$ ,  $N_{P_{ij}^*}$ , and  $N_{E^*}$ . Here, the output  $N_{P_{ij}^*}$  is used to regulate the constitutive relation loss between the stress tensor  $P_{ij}^*(u_i^*, E^*)$ , computed from the estimated  $u_i^*$  and  $E^*$ , and stress tensor  $N_{P_{ij}^*}$  that directly estimated from the network. On the other hand, FCNN III, IV, and V are designed only to estimate  $N_{u_i^*}$  and  $N_{E^*}$  without ensuring a balanced constitutive relation loss.

To provide more details into FCNN I and II, FCNN I comprises two subnetworks. The first subnetwork has a shared network of two hidden layers with 50 neurons per layer. The shared network is split into two independent networks, each composed of two hidden layers with 50 neurons per layer. Each of the subnetworks predicts one of the displacement components (*i.e.*,  $N_{u_x^*}$  and  $N_{u_y^*}$ ). The second subnetwork is a shared network consisting of five hidden layers with 75 neurons per layer that outputs  $N_{E^*}$  and  $N_{P_{ij}^*}$ . In FCNN II, we similarly formulated two independent networks, each consisting of five hidden layers with 75 neurons per layer. The first independent network outputs the displacement components. In contrast, the second outputs the elastic moduli and the stress components, as the elastic moduli and stresses would share similar features given their direct mathematical relationship.

Regarding FCNN III, IV, and V, in FCNN III, we constructed a two-hidden layer shared network to connect the displacement components and elastic moduli. The shared network is subsequently split into three independent networks with three hidden layers with 25 neurons per layer to individual features in the displacement component and elastic moduli. FCNN IV consists of three independent networks, each with five hidden layers and 25 neurons per layer. FCNN V represents the simplest form of neural network architecture, in which one shared network is formulated to estimate  $N_{u_i^*}$  and  $N_{E^*}$ .

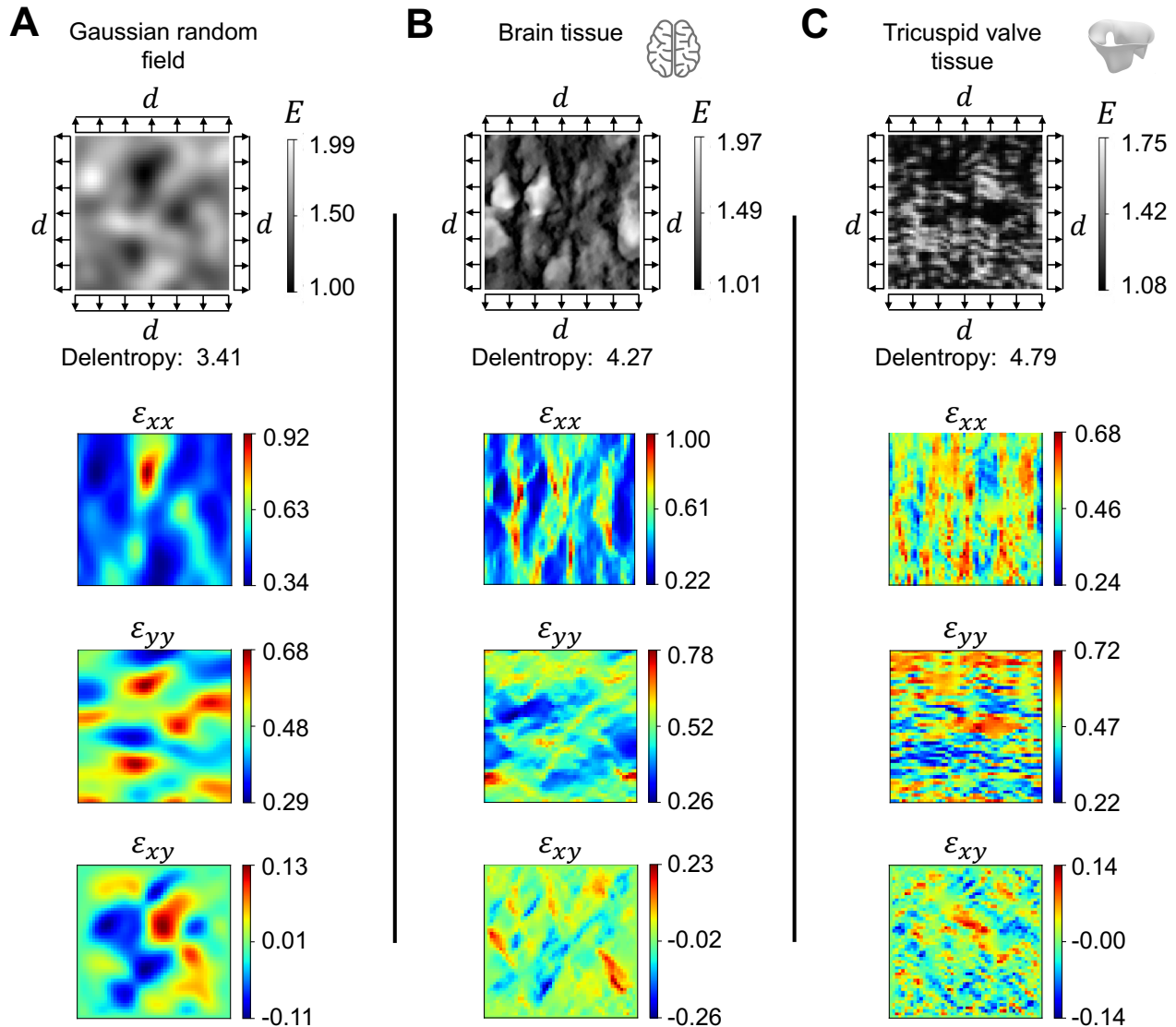
In our analyses, we considered the strong form of linear momentum equations as the governing equation of the physical system

$$P_{ij,i} = 0,$$

where  $P$  is the first Piola-Kirchhoff stress described in Section. 5.1.

### 2.2.2 Fourier-feature PINNs

Standard PINNs often experience difficulties learning the parameter distribution of the materials with complex and random structural patterns. Seminal works have demonstrated the effectiveness of Fourier-feature transforms in solving benchmark PDEs problems and complex ordinary differential equations<sup>62,68</sup>. As such, we extended our standard PINN architecture with Fourier-feature transforms to decompose the complex structural features into multiple layers to learn the high-frequency structural features, aiming to capture the intricate patterns through a multi-scale approach.



Reference strain fields for inferring the full-field elastic modulus

**Figure 1. Heterogeneous material examples.** The examples are presented in the undeformed configuration of unit square specimens. These examples represent the unknown elastic properties distribution of soft tissue that we seek to identify using PINNs. The structural complexity of the sample was quantified using Delentropy; higher values indicate greater complexity. **(A)** The structural pattern is synthetically generated using a GRF<sup>78</sup>. **(B)** The representation of the brain tissue microstructure was adapted from Koos et al.<sup>79</sup>. **(C)** The fibrosis network of the tricuspid valve was adapted from Weinberg et al.<sup>80</sup>. Equibiaxial deformation of magnitude  $d$  was applied to the undeformed configuration using FEA to obtain the ground truth strain distribution. We prescribed 40% equibiaxial stretch to the specimen (*i.e.*, 20% to each side of the boundary) and estimated the resulting Green-Lagrangian strain using FEniCS<sup>83</sup>. The strain data were used as ground truth reference data to identify the “unknown” elastic moduli in PINNs inversely.

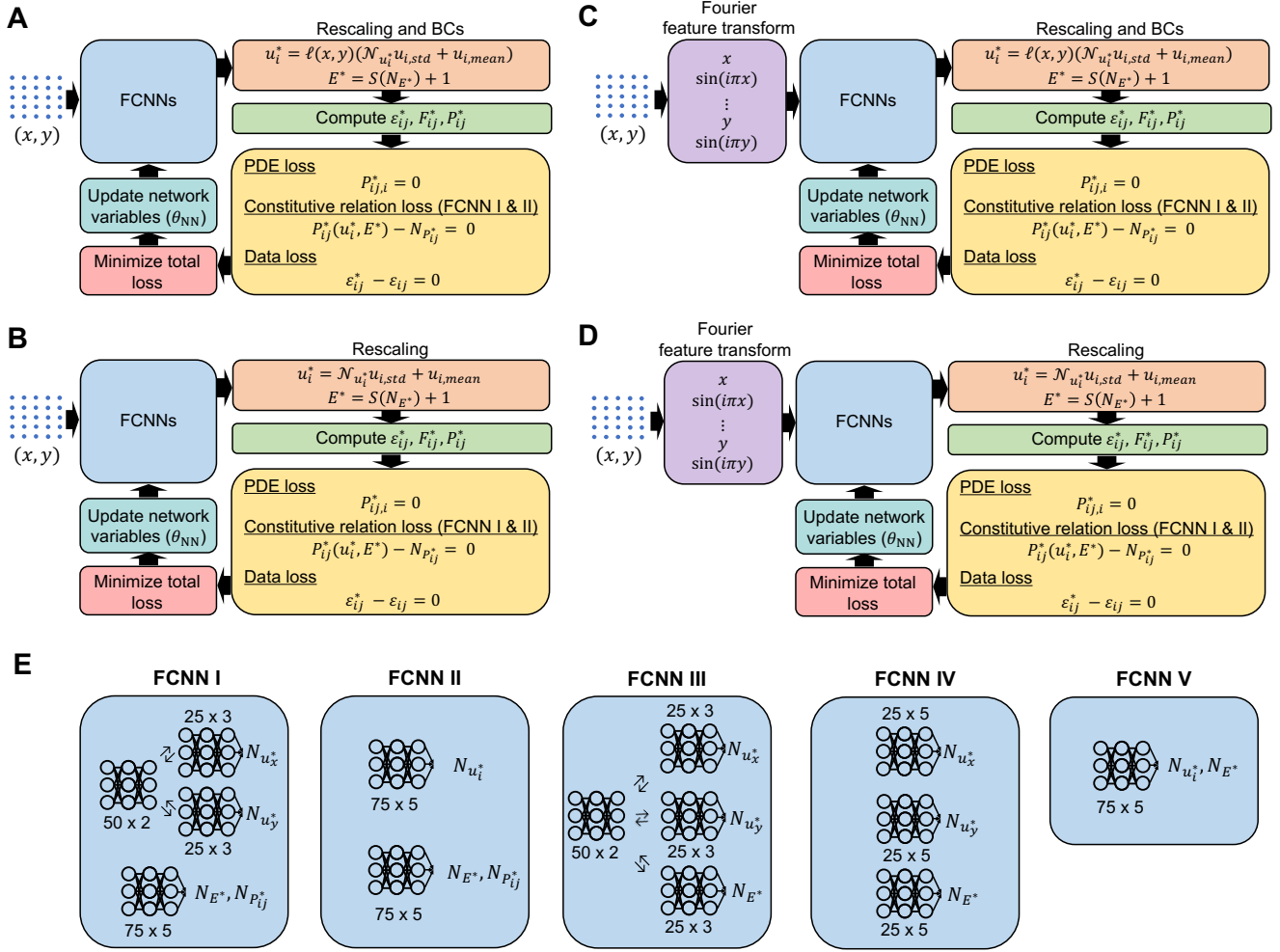


**Figure 2. Network architecture overview.** We established four PINN variants to examine the effectiveness of PINNs in identifying the heterogeneous elastic properties of hyperelastic materials. **(A)** A standard PINN with boundary conditions embedded as hard constraints. **(B)** A standard PINN without enforcing boundary conditions. **(C)** A Fourier-feature PINN with boundary conditions embedded as hard constraints. **(D)** A Fourier-feature PINN without enforcing boundary conditions. **(E)** For each PINN variant, we experimented with five types of FCNN architectures to determine the best arrangement of independent neural networks to achieve accurate estimates of the elastic properties distribution in complex materials. In Fourier-feature PINNs, the input coordinates of the PDE training points are mapped to a total of 10 Fourier modes (five Fourier modes for  $x$  and five Fourier modes for  $y$ ).

We transformed the input coordinates through a Fourier-feature mapping with five Fourier modes per input variable before feeding it to the fully connected feedforward network, as depicted in Fig. 2. In particular, we retained the spatial coordinates,  $x$  and  $y$ , with additional terms of  $\sin(i\pi x)$  and  $\sin(i\pi y)$  for  $i = 1, 2, \dots, 5$ . Incorporating these features into the network can facilitate the learning of similar features and thus may reduce the computational difficulties for feature extraction. These very general Fourier features were found to provide good results. Additional hyperparameter fine-tuning could be applied for better results, such as  $\sin(\pi xy)$ , but was not utilized in these cases for simplicity and proof of concept.

### 2.3 Overall findings on the computational experiments

This section discusses the prediction accuracies of the proposed architectures in estimating the complex elastic property distributions of soft materials that undergo large deformation. The means and standard deviations of the  $L^2$  relative errors of the estimated elastic modulus distribution of each example are shown in Figs. 3A to C. Each analysis was repeated with varying random seeds five times to ensure solution consistency. The FCNN that produces less than 5% average estimation errors are highlighted in bold. Furthermore, the architectures that consistently met the accuracy requirements across all three examples are underlined. The average computation time for each network architecture across the three examples and the five repeated tests are reported in Fig. 3D.

In the first example (Fig. 3A), PINN models A and B produced similar prediction accuracy across all five FCNN architectures. The difference in  $L^2$  relative error between PINN models A and B was less than 1% for each FCNN architecture. On the contrary, four out of five FCNN architectures had higher  $L^2$  relative errors in Fourier-feature PINN model C than D, suggesting, in this example, Fourier-feature PINNs provide more accurate estimates of the elastic parameter distribution when the boundary conditions were unconstrained.

In the second example (Fig. 3B), while FCNN III and V with PINN model A marginally outperformed those with PINN model B, the  $L^2$  relative errors in FCNN architectures I, II, and IV were significantly higher with PINN models A than B, with differences in errors range from 1.35% to 5.99%. In contrast, Fourier-feature PINN model C produced comparable or better prediction than Fourier-feature PINN model D, with as much as 20.28% lower in  $L^2$  relative error across the five FCNN architectures. In addition, FCNN III, IV, and V yielded the lowest  $L^2$  relative errors (2.99%, 2.77%, and 2.61%, respectively) in Fourier-feature PINNs model C compared to the other models.

In the third example (Fig. 3C), we observed similar  $L^2$  relative error trends as those in Fig. 3B. Fourier-feature PINNs performed better than standard PINNs in this example. Moreover, Fourier-feature model C provided highly accurate estimations of the elastic parameter distribution with  $L^2$  errors less than 5% across all FCNN architectures. In general, neural network architectures that enforce constitutive relations (FCNN I and II) demonstrate superior prediction accuracy in both standard PINNs and Fourier-feature PINNs when compared to architectures that do not enforce constitutive relations (FCNN III, IV, and V). This observation highlights the importance of considering the underlying physics and problem characteristics when designing and training PINNs.

While we expected the network prediction accuracy would improve with additional information on the boundary. However, our experiments showed that embedding boundary conditions in the inverse analysis did not significantly improve the prediction of the unknown material parameters across the three examples in the standard PINNs. Conversely, enforcing boundary constraints substantially improved the estimation accuracy in the second example using Fourier-feature PINNs while producing comparable prediction accuracy in the first and third examples. These unexpected results could be because the network has learned the deformation boundary conditions from the provided strain reference data. Therefore, enforcing the boundary may not provide additional information to guide the optimization.

**A**

$L^2$  relative errors (%) 

Network architecture	Standard PINNs		Fourier-feature PINNs	
	A	B	C	D
I	<b>0.80 ± 0.22</b>	<b>0.67 ± 0.70</b>	6.02 ± 3.14	5.06 ± 2.02
II	1.03 ± 0.23	<u>0.45 ± 0.11</u>	<u>4.20 ± 1.23</u>	5.76 ± 3.35
III	<b>0.49 ± 0.30</b>	1.39 ± 0.24	5.76 ± 0.82	<b>0.61 ± 0.16</b>
IV	1.62 ± 0.62	2.38 ± 0.90	<u>2.85 ± 1.08</u>	1.30 ± 1.02
V	1.31 ± 0.20	0.50 ± 0.23	13.09 ± 1.36	<b>1.18 ± 0.06</b>

**B**

$L^2$  relative errors (%) 

Network architecture	Standard PINNs		Fourier-feature PINNs	
	A	B	C	D
I	14.75 ± 5.78	9.01 ± 6.93	<b>3.05 ± 0.22</b>	<b>1.93 ± 0.21</b>
II	9.11 ± 8.42	<u>3.12 ± 0.87</u>	<u>2.32 ± 0.30</u>	<b>2.18 ± 0.27</b>
III	12.87 ± 3.40	14.88 ± 0.85	<b>2.99 ± 0.13</b>	19.93 ± 6.11
IV	18.16 ± 8.19	16.81 ± 2.80	<u>2.77 ± 0.43</u>	11.49 ± 10.22
V	<b>3.41 ± 1.75</b>	5.59 ± 0.44	<b>2.61 ± 0.13</b>	22.89 ± 3.53

**C**

$L^2$  relative errors (%) 

Network architecture	Standard PINNs		Fourier-feature PINNs	
	A	B	C	D
I	5.78 ± 5.34	<b>3.07 ± 0.13</b>	<b>2.90 ± 0.19</b>	<b>4.53 ± 0.20</b>
II	7.01 ± 5.38	<u>3.05 ± 0.37</u>	<u>3.95 ± 0.34</u>	<b>4.50 ± 0.12</b>
III	10.24 ± 2.78	11.35 ± 1.57	<b>2.78 ± 0.10</b>	5.92 ± 1.15
IV	8.04 ± 3.52	10.72 ± 2.47	<u>4.23 ± 1.03</u>	7.51 ± 1.02
V	10.49 ± 0.82	5.85 ± 1.31	<b>3.63 ± 0.16</b>	<b>4.46 ± 0.21</b>

**D**

Average computational time (hours)

Network architecture	Standard PINNs		Fourier-feature PINNs	
	A	B	C	D
I	10.4 ± 0.14	9.0 ± 0.13	13.6 ± 0.18	12.4 ± 0.25
II	9.3 ± 0.37	8.0 ± 0.12	11.8 ± 0.23	10.7 ± 0.36
III	8.9 ± 0.12	7.6 ± 0.18	13.5 ± 0.45	10.8 ± 0.12
IV	11.1 ± 0.17	9.7 ± 0.15	14.1 ± 0.24	12.9 ± 0.16
V	5.4 ± 0.09	4.4 ± 0.03	8.6 ± 0.16	7.5 ± 0.09

**Figure 3. Overall results.** We conducted five evaluations for each PINN and FCNN architecture variant. (A–C) The mean and standard deviations of  $L^2$  relative errors of the PINN-estimated full-field elastic moduli. The network architectures that produced less than 5%  $L^2$  relative errors are highlighted in bold. The architectures that consistently met the accuracy requirements across all three examples are underlined. Among the three network architectures that demonstrated high estimation accuracy across the examples, Network architecture IIB was the most computationally efficient. (D) The computational time for each PINN architecture.

It is worth noting that Fourier-feature PINNs resulted in better estimations of elastic moduli in the second and third examples, but poorer estimations in the first example. This implies that the second and third examples display trigonometric features in their underlying microstructure, which are visibly apparent in the second and more subtle in the third. Therefore, the Fourier-feature transform provided additional guidance to the training process, subsequently improving the prediction accuracy. However, the first example did not seem to contain the same features. As a result, the Fourier-feature transform had a negative impact on the estimation of elastic property distribution.

Out of the 20 network architectures tested, the network architectures IIB, IIC, and IVC were found to produce highly accurate estimations consistently across the three examples. The results suggest that partitioning output variables into separate independent networks, based on their shared features, may substantially enhance prediction accuracy. Among these three selected models, network architecture IIB provided accurate estimates of the elastic moduli, with average  $L^2$  relative errors of 0.45%, 3.12%, and 3.05% for the three examples, while also being the fastest in terms of computational time.

Regarding computational time, Fourier-feature PINNs took longer training time than standard PINNs. This is because of the additional neural network parameters introduced from the Fourier-feature mapping. Additionally, enforcing hard boundary conditions led to longer computational time in both standard and Fourier-feature PINNs. Among the PINN and Fourier-feature PINN models, model B required the least amount of training time overall, and among different architectures, FCNN architecture V required the least training time.

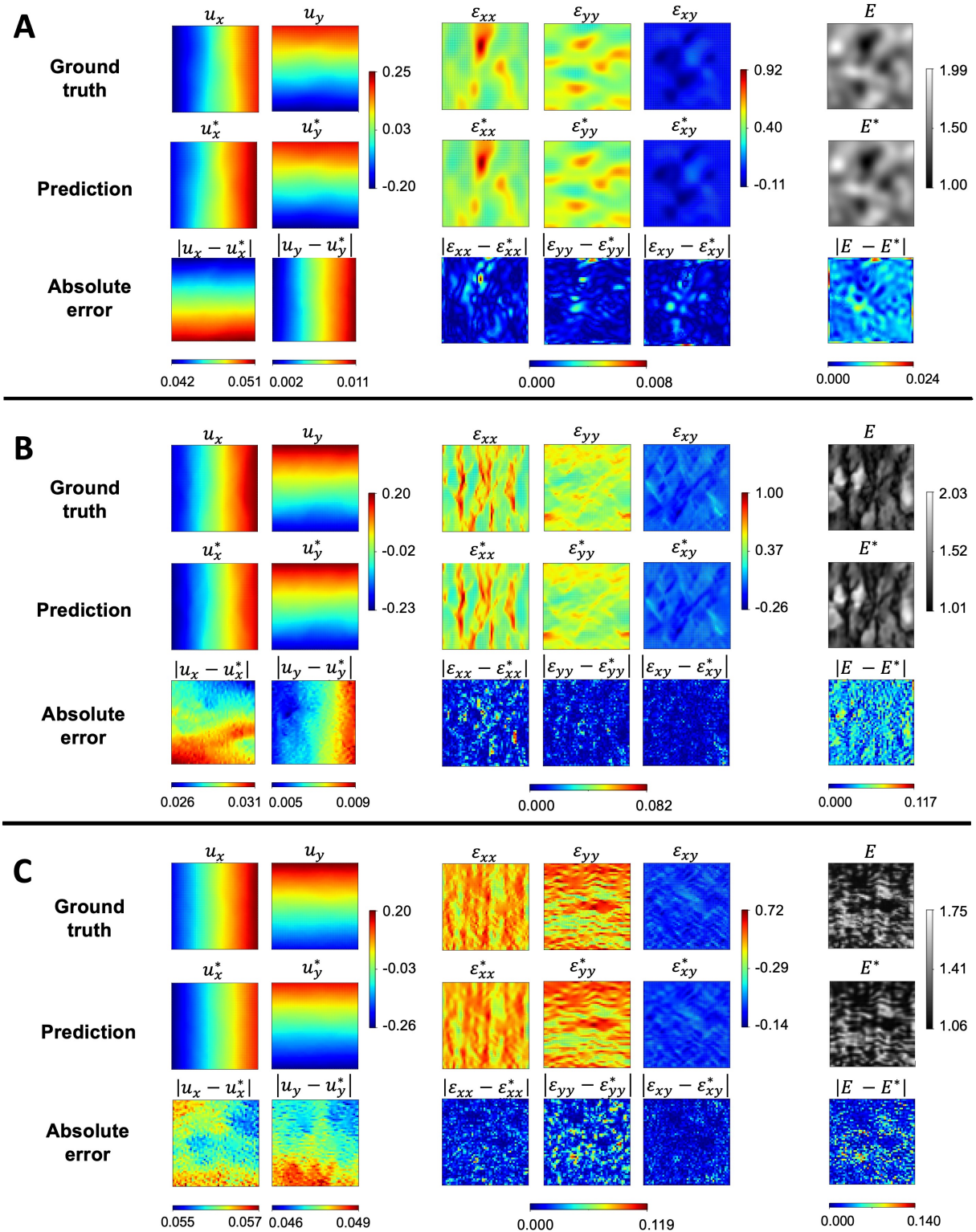
## 2.4 Displacement, strain, and elastic modulus estimation

Fig. 4 presents the estimated displacements, strain, and elastic modulus distribution of the three examples using network architecture IIB. The absolute relative errors between the PINN estimation and FEA ground truth are also provided for comparison. Despite the displacement boundaries being unconstrained in this network architecture, this PINN model demonstrated highly accurate estimation of the displacement, strain, and elastic parameter distribution across the three examples with relative errors up to  $\mathcal{O}(10^{-2})$  for full-field displacements and strains and  $\mathcal{O}(10^{-1})$  for the elastic moduli. These results indicate the consistency and generality of the proposed neural network architecture for estimating the mechanical properties of complex microstructures.

As the elasticity fields become more complex, with increasing local features, the corresponding strain fields become more complex. Consequently, we observed higher absolute errors associated with both the strain and elastic modulus in the second and third examples. In the first example, the maximum absolute errors of the strain and elasticity field were 0.01 and 0.02, respectively. However, these errors were 0.08 and 0.12 in the second example, and 0.12 and 0.14 in the third example. It is worth noting that increasing the size of the FCNN architecture may help resolve the finer features in the elasticity map, leading to better accuracy in the more complex examples.

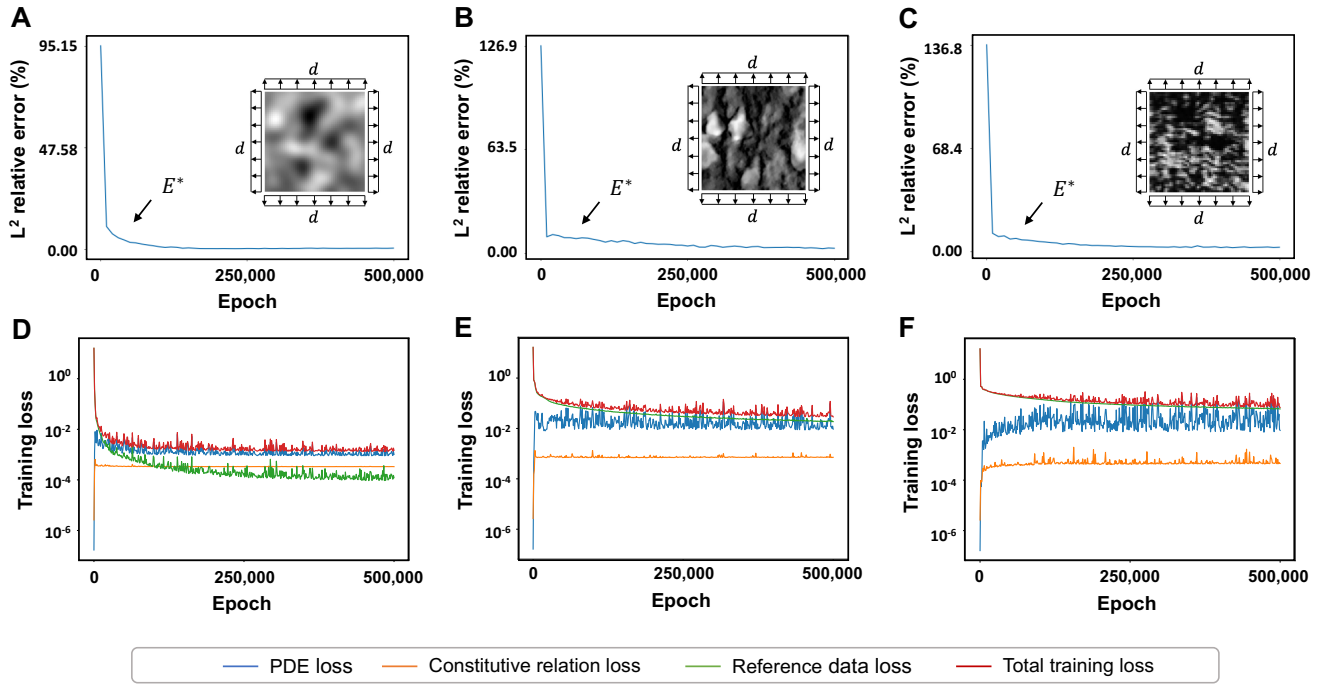
## 2.5 Convergence behavior of the PINN training

Fig. 5 shows the convergence histories of the elastic moduli and the training loss of each example. As shown, the training procedures and the estimated elastic moduli converge rapidly within the user-defined duration of  $5 \times 10^5$  epochs. Figs. 5A and D demonstrate the convergence evolution of the training procedure for the first example. The  $L^2$  relative error of the elastic moduli first decays to below 5% at around 4,000 iterations. The estimated elastic moduli continue to approach the FEA ground truth for the remaining iterations, reaching a final relative error of 0.56%. Similarly, the total training loss decreases from  $\mathcal{O}(10^{-1})$  to  $\mathcal{O}(10^{-3})$  within the first 150,000 iterations. The PDE and constitutive relation losses have reached a plateau immediately at around 1,000 iterations and consistently maintain  $\mathcal{O}(10^{-3})$  and



**Figure 4. PINN predictions and pointwise error.** The FEA ground truth, PINN estimation (denoted with superscript  $*$ ), and the absolute errors of displacement, strain, and elastic modulus distribution for examples (A), (B), and (C) are shown. The PINN architecture effectively resolves the local features of complex strain and elastic modulus fields. The absolute errors were up to  $\mathcal{O}(10^{-2})$  for the displacement and up to  $\mathcal{O}(10^{-1})$  for the strain and elasticity fields.

$\mathcal{O}(10^{-4})$  relative error. Similar patterns are observed in the second example (Figs. 5B and E) and C (Figs. 5C and F). The  $L^2$  relative error of the elastic moduli in the second example decays to below 5% at around 250,000 iterations and steadily reduces the error to 2.91% at the end of the training. The  $L^2$  relative error of the elastic moduli in example C decays to below 5% at around 150,000 iterations and reduces the error to 2.78% at the end of the training. Across the three examples, total training loss converging behavior aligns more with data loss, suggesting that the training procedure is more sensitive to deviation in the strain reference data.



**Figure 5. PINN training behavior.** The  $L^2$  relative errors of the full-field elastic parameters and the training loss convergence history are presented. We observed rapid convergences in the  $L^2$  relative errors across all three examples. The  $L^2$  relative errors of the elastic parameter predictions reduced below 5% within 4,000 epochs in the first example, 250,000 epochs in the second example, and 150,000 epochs in the third example. The constitutive relation and PDE losses reach plateaus almost immediately at the beginning of the training across all three examples, while the total training loss follows the same decay rate as the reference data loss.

### 3 Discussion

In the current work, we proposed a novel approach to accurately uncover the heterogeneous elastic property of hyperelastic materials using PINNs. We experimented with five FCNN architectures in both methods and identified a top-performing PINN architecture that efficiently produced the best estimations across all examples. We used the same hyperparameters (*e.g.*, loss weights, learning decay rate, and optimization algorithm) in each analysis to ensure generality and that the estimated results are independent of parameter tuning. We have selected network architecture IIB as the top-performing network architecture as it consistently yielded accurate estimations of the full-field elastic modulus, with  $L^2$  relative errors of  $0.43 \pm 0.11\%$ ,  $3.28 \pm 0.93\%$ , and  $3.09 \pm 0.41\%$ , for the three examples respectively, while also took the least computational time.

The positive results of our work have opened new opportunities to accurately quantify the elasticity

map in clinical strain-based ultrasound elasticity imaging. Shear wave elastography is a common imaging technique for detecting cancerous tissue by measuring tissue elasticity maps through shear wave velocity. However, commercially available US elastography systems assume that soft tissues have homogeneous and incompressible mechanical properties, despite the high degree of heterogeneity in soft tissue properties<sup>84</sup>. This results in an underestimation of tissue stiffness and less accurate predictions. Our work demonstrated that our architecture can accurately estimate the elastic properties distribution using only strain as the training data. The unique characteristics of PINNs, which allow for the estimation of the local stress and elastic moduli, help circumvent the assumption in the tissue behavior and may provide a more accurate quantitative measure of the stiffness map, therefore, leading to a more accurate diagnosis.

Our method demonstrates promising potential extension to microstructure and material properties studies in a compact, flexible, unified framework. Our network architecture offers immense flexibility to integrate additional empirical data and physical principles relevant to the problem. While the current study focuses on the micromechanical properties of soft materials, our architecture can be easily extended to include data such as the temperature field and thermodynamics conservation laws to study the material microstructure progress during crack propagation, helping accelerate progress in material designs and optimization.

While we have not been focused on optimizing the computational time of our analyses, there are a few approaches one could make to reduce the computational cost. First, our studies adopted the FE nodal coordinates (a total of 5101 nodes) as the PDE training points and reference data collocation points. One may experiment with the effect of reducing the number of training points on estimation accuracy<sup>55,85,86</sup>. Second, as noted in Section 2.5, the training loss appears to converge rapidly within the first 250,000 iterations of the analysis; depending on the level of accuracy desired, one may also reduce the number of iterations needed. Third, we used the Adam optimizer in our training; one may experiment with the use of second-order optimizers<sup>64,87</sup> to achieve faster estimation convergence while maintaining the same order of accuracy. Lastly, there has been active research on methods to reduce GPU memory consumption and wall time in physics-informed machine learning, such as mixed precision<sup>88</sup>.

In our work, we have chosen three examples with complex morphology to encapsulate the wide variety of structural patterns in soft tissues. It should be noted that the depth and width of FCNNs may need to be adjusted to accommodate the increasing complexity of the tissue structure. Here, we quantified the structural complexity of the tissue sample using Delentropy. We hope this measure will help guide the designs of the FCNN architecture tailored to individual tissue specimens in future studies.

## 4 Conclusions

In conclusion, we have identified a general network architecture that produces highly accurate elastic moduli estimates for complex heterogeneous materials, with  $L^2$  relative error less than 5% across the examples in our study. The results of this work provide a promising framework for identifying the heterogeneous elastic properties in soft materials from images, paving the way to accelerate research progress in material designs, material optimization, and medical applications.

## 5 Methods

In this work, we investigated the accuracy of standard PINNs and Fourier-feature PINNs in estimating the elastic properties of heterogeneous materials in 2D. Each PINN method consisted of two variants: one with boundary conditions embedded as hard constraints and one without. Additionally, we established five network architectures with a unique arrangement of independent neural networks. A total of 20 neural network architectures were applied to each example to determine the most effective architecture for

predicting the elastic modulus distribution in complex materials. Details on the data generation and details pertaining to the neural network architectures are provided in Sections 5.1 to 5.3.

## 5.1 Reference data generation

In tensile tests, the displacement fields often do not provide sufficient local data to uncover the fine features in heterogeneous materials. Therefore, strains ( $\varepsilon_{ij}$ ) were used to regulate the data loss and train our neural networks. We generated the strain fields using FEA. The first step was prescribing the heterogeneous structure and elastic properties of a finite element mesh. In the first example, we discretized a unit square domain into 10,000 triangular elements and 5,101 nodes in FEniCS<sup>83</sup>. The heterogeneous pattern was generated by assigning random intensity values to the nodal coordinates using a mean-zero GRF defined as

$$f(x) \sim \mathcal{G} \mathcal{P}(0, k_l(x_1, x_2)),$$

where  $k_l(x_1, x_2)$  is the Gaussian kernel and  $l$  is the correlation length. We chose a radial basis kernel function with  $l = 0.1$  in this work.

In the second and third examples, we utilized the tissue microstructure images obtained from Koos et al.<sup>79</sup> and Weinberg et al.<sup>80</sup> to map the complex microstructure patterns to a finite element mesh. First, we cropped a section of the image and transformed the dimension to a unit square. Then, we used min-max normalization to scale the image intensity values to a range from 0 to 1. We followed the same procedure as the first example, wherein a unit-square geometry was established in FEniCS<sup>83</sup>, and discretized the domain into 10,000 cells and 5,101 nodes. Finally, we interpolated the image intensity using cubic interpolation to map the heterogeneous feature of the brain and tricuspid valve leaflet tissue onto the finite element mesh.

In these examples, Young's modulus of each element was calculated based on the intensity at the nodal coordinates following

$$E_{ele} = \sum_{i=1}^3 f(x_i) + 1,$$

where  $f(x_i)$  is the pixel intensity associated with node  $i$  on the triangle element; a higher intensity value indicates greater stiffness. We considered a compressible isotropic Neo-Hookean hyperelastic constitutive model<sup>89</sup>, where the first Piola-Kirchhoff stress is formulated as

$$P = \frac{\partial \Psi}{\partial F} = \mu F + [\lambda \log(J) - \mu] F^{-T}.$$

Herein,  $\lambda$  and  $\mu$  are the Lamé's elasticity parameters. Further,  $\Psi$  is the strain energy density function expressed as

$$\Psi(I_1, J) = \frac{1}{2} \lambda [\log(J)]^2 - \mu \log(J) + \frac{1}{2} \mu (I_1 - 2),$$

where  $I_1 = \text{trace}(F^T \cdot F)$ ,  $F_{ij} = \delta_{ij} + u_{i,j}$ , and  $u_{i,j}$  is the displacement vector. The Green-Lagrangian strain is defined as

$$\varepsilon_{ij} = \frac{1}{2} (F_{ki} F_{kj} - \delta_{ij}).$$

In the current work, we followed a plane-strain formulation:

$$\lambda = \frac{E\nu}{(1+\nu)(1-2\nu)}, \quad \text{and} \quad \mu = \frac{E}{2(1+\nu)},$$

where we assumed  $\nu = 0.3$ . The finite element mesh was deformed by applying an equibiaxial displacement ( $d = 0.2$ ) to the boundaries, as shown in Fig. 1.

## 5.2 Sample complexity

We used Delentropy<sup>81,82</sup> to analyze the spatial structure and pixel co-occurrence of the tissue image and evaluate the complexity of the tissue structural pattern. The Delentropy is expressed as

$$DE = -\frac{1}{2} \sum_{j=0}^{J-1} \sum_{i=0}^{I-1} p_{i,j} \log_2 p_{i,j},$$

where  $p_{i,j}$  is the deldensity probability density function and  $I$  and  $J$  are the number of discrete cells in the  $x$  and  $y$  dimensions of the probability density function. The deldensity probability density function is computed as

$$p_{i,j} = \frac{1}{4WH} \sum_{w=0}^{W-1} \sum_{h=0}^{H-1} \delta_{i,d_x}(w,h) \delta_{j,d_y}(w,h),$$

where  $W$  and  $H$  are the width and height of the image, respectively. The Kronecker delta,  $\delta$ , describes the binning operation for generating a 2D histogram for the image.  $d_x$  and  $d_y$  are the derivative of the kernels in  $x$  and  $y$  directions, respectively. The local derivatives were estimated by computing the central difference corresponding to the convolution kernel of  $[[[-1, 0, 1], [-1, 0, 1], [-1, 0, 1]]]$ .

## 5.3 PINNs for heterogeneous material properties identification

As an extension to prior work on utilizing PINNs to determine the macroscopic constitutive parameters in linear and hyperelastic materials<sup>54,55</sup>, we demonstrate a proof-of-concept study to identify the full-field elastic properties across the 2D geometric domain. Our work aims to facilitate future studies to better understand the interconnection between material microscopic properties and its macroscopic mechanical functions. All PINNs models were constructed using the DeepXDE library<sup>85</sup>, and the code is publicly available in the GitHub repository <https://github.com/lu-group/pinn-heterogeneous-material>.

### 5.3.1 Output transform

Rescale network outputs magnitudes to the scale of  $\mathcal{O}(1)$  can help improve the optimization process. We normalized the displacement outputs by the mean and standard deviation obtained from the finite element analysis. Subsequently, we implemented hard constraint displacement boundary conditions in the same fashion described in Refs.<sup>53,55</sup>. The transformation of the displacement vectors in a compact form is expressed as

$$u_i^* = \ell(\mathbf{x})(\mathcal{N}_{u_i^*} u_{i,\text{std}} + u_{i,\text{mean}}),$$

where  $u_i^*$  is the final PINN displacement vector,  $\ell(\mathbf{x})$  is the hard constraint function,  $\mathcal{N}_{u_i^*}$  is the normalized PINN displacement vector,  $u_{i,\text{std}}$  and  $u_{i,\text{mean}}$  are the mean and standard deviation of the reference displacement vectors. Further, we constrained the range of  $E$  to physically realistic values using a sigmoid function

$$E^* = \frac{4}{1 + e^{-\mathcal{N}_{E^*}}} + 1.$$

### 5.3.2 Loss functions

The training process aims to optimize the network parameters,  $\theta_{\text{NN}}$ , in

$$\theta_{\text{NN}}^* = \arg \min_{\theta_{\text{NN}}} \mathcal{L}(\theta_{\text{NN}}),$$

where  $\mathcal{L}(\theta_{\text{NN}})$  is the loss function that measures the total error concerning the PDEs (the momentum balance), constitutive relation, and reference data loss; the boundary condition loss is eliminated since we impose the boundary conditions using hard constraints. The total loss function for FCNN I and II is defined as

$$\mathcal{L}(\theta_{\text{NN}}, \theta_{\text{mat}}) = w_{\text{PDEs}} \mathcal{L}_{\text{PDEs}} + w_{\text{Constitutive relations}} \mathcal{L}_{\text{Constitutive relations}} + w_{\text{Data}} \mathcal{L}_{\text{Data}},$$

where  $w_{\bullet}$  is the weight associated with its corresponding loss term  $\mathcal{L}_{\bullet}$ . The loss terms  $\mathcal{L}_{\text{Data}}$  compute the mean squared error of predicted results on the collocation points and reference data, respectively. While displacement and strain data were available, we only used strains to facilitate data loss because including displacements did not improve model prediction.  $\mathcal{L}_{\text{PDEs}}$  and  $\mathcal{L}_{\text{Constitutive relations}}$  computes the mean squared error of the PDE residuals and constitutive behavior loss over the spatial domain. The weights associated with PDEs, Constitutive relation, and data loss were 1,  $E^2$ , and 100, respectively. The total loss function for FCNN III to V is reduced to

$$\mathcal{L}(\theta_{\text{NN}}, \theta_{\text{mat}}) = w_{\text{PDEs}} \mathcal{L}_{\text{PDEs}} + w_{\text{Data}} \mathcal{L}_{\text{Data}}.$$

Without loss of generality, we adopted the Swish activation function across all analyses and trained the network with 500,000 iterations with Adam optimizer and learning rate as 0.001 in all studies.

## Author contributions

W. W.: Conceptualization, Methodology, Formal analysis, Visualization, Writing – Original Draft; M. D.: Conceptualization, Writing – Review & Editing; K. T. T.: Conceptualization, Writing – Review & Editing; M. A. J.: Conceptualization, Resources, Writing – Review & Editing; L. L.: Conceptualization, Writing – Review & Editing, Supervision. All authors discussed the results.

## Acknowledgments

This work was supported by the Cora Topolewski Pediatric Valve Center at the Children’s Hospital of Philadelphia, an Additional Ventures Expansion Award, the National Institutes of Health, and the U.S. Department of Energy. WW was initially supported by NHLBI T32 HL007915 and transitioned to NHLBI K25 HL168235. MAJ was supported by NIH R01 HL153166, an Additional Ventures Single Ventricle Grant, and the Topolewski Endowed Chair in Pediatric Cardiology. MD and LL were supported by the U.S. Department of Energy [DE-SC0022953].

## Competing interests

All authors declare no financial or non-financial competing interests.

## Code availability

The code for this study is available in the GitHub repository <https://github.com/lu-group/pinn-heterogeneous-material>.

## References

1. Wei, J. *et al.* Bioinspired additive manufacturing of hierarchical materials: From biostructures to functions. *Research* **6**, 0164, DOI: <https://doi.org/10.34133/research.0164> (2023).

2. Lee, D., Chen, W. W., Wang, L., Chan, Y.-C. & Chen, W. Data-driven design for metamaterials and multiscale systems: A review. *Adv. Mater.* **n/a**, 2305254, DOI: <https://doi.org/10.1002/adma.202305254> (2023).
3. Xuan, Y. *et al.* Regional biomechanical and failure properties of healthy human ascending aorta and root. *J. Mech. Behav. Biomed. Mater.* **123**, 104705, DOI: <https://doi.org/10.1016/j.jmbbm.2021.104705> (2021).
4. Burris, N. S. *et al.* Vascular deformation mapping for CT surveillance of thoracic aortic aneurysm growth. *Radiology* **302**, 218–225, DOI: <https://doi.org/10.1148/radiol.2021210658> (2022). PMID: 34665030.
5. Lin, S. *et al.* Aortic local biomechanical properties in ascending aortic aneurysms. *Acta Biomater.* **149**, 40–50, DOI: <https://doi.org/10.1016/j.actbio.2022.06.019> (2022).
6. Vander Linden, K. *et al.* Stiffness matters: Improved failure risk assessment of ascending thoracic aortic aneurysms. *JTCVS Open* **16**, 66–83, DOI: <https://doi.org/10.1016/j.xjon.2023.09.008> (2023). Precision Therapy in Lung Cancer.
7. Chang, Z., Zhang, J., Liu, Y., Gao, H. & Xu, G.-K. New mechanical markers for tracking the progression of myocardial infarction. *Nano Lett.* **23**, 7350–7357, DOI: <https://doi.org/10.1021/acs.nanolett.3c01712> (2023).
8. Sadeghinia, M. J. *et al.* Mechanical behavior and collagen structure of degenerative mitral valve leaflets and a finite element model of primary mitral regurgitation. *Acta Biomater.* **164**, 269–281, DOI: <https://doi.org/10.1016/j.actbio.2023.03.029> (2023).
9. Micalet, A., Moeendarbary, E. & Cheema, U. 3D in vitro models for investigating the role of stiffness in cancer invasion. *ACS Biomater. Sci. & Eng.* **9**, 3729–3741, DOI: <https://doi.org/10.1021/acsbiomaterials.0c01530> (2023).
10. Seifert, A. W. *et al.* Skin shedding and tissue regeneration in african spiny mice (*Acomys*). *Nature* **489**, 561–565, DOI: <https://doi.org/10.1038/nature11499> (2012).
11. Maden, M. *et al.* Perfect chronic skeletal muscle regeneration in adult spiny mice, *Acomys cahirinus*. *Sci. Reports* **8**, 8920, DOI: <https://doi.org/10.1038/s41598-018-27178-7> (2018).
12. Notari, M. *et al.* The local microenvironment limits the regenerative potential of the mouse neonatal heart. *Sci. Adv.* **4**, eaao5553, DOI: <https://doi.org/10.1126/sciadv.aao5553> (2018).
13. Harn, H. I.-C. *et al.* Symmetry breaking of tissue mechanics in wound induced hair follicle regeneration of laboratory and spiny mice. *Nat. Commun.* **12**, 2595, DOI: <https://doi.org/10.1038/s41467-021-22822-9> (2021).
14. Paszek, M. J. *et al.* Tensional homeostasis and the malignant phenotype. *Cancer Cell* **8**, 241–254, DOI: <https://doi.org/10.1016/j.ccr.2005.08.010> (2005).
15. Engler, A. J., Sen, S., Sweeney, H. L. & Discher, D. E. Matrix elasticity directs stem cell lineage specification. *Cell* **126**, 677–689, DOI: <https://doi.org/10.1016/j.cell.2006.06.044> (2006).
16. Sommakia, S., Lee, H. C., Gaire, J. & Otto, K. J. Materials approaches for modulating neural tissue responses to implanted microelectrodes through mechanical and biochemical means. *Curr. Opin. Solid State Mater. Sci.* **18**, 319–328, DOI: <https://doi.org/10.1016/j.cossms.2014.07.005> (2014). Neuroengineering Materials.

17. Wilson, H. M. Modulation of macrophages by biophysical cues in health and beyond. *Discov. Immunol.* **2**, kyad013, DOI: <https://doi.org/10.1093/discim/kyad013> (2023).
18. Wu, H. *et al.* Progressive pulmonary fibrosis is caused by elevated mechanical tension on alveolar stem cells. *Cell* **180**, 107–121, DOI: <https://doi.org/10.1016/j.cell.2019.11.027> (2020).
19. Henderson, N. C., Rieder, F. & Wynn, T. A. Fibrosis: from mechanisms to medicines. *Nature* **587**, 555–566, DOI: <https://doi.org/10.1038/s41586-020-2938-9> (2020).
20. Sommer, G. *et al.* Biomechanical properties and microstructure of human ventricular myocardium. *Acta Biomater.* **24**, 172–192, DOI: <https://doi.org/10.1016/j.actbio.2015.06.031> (2015).
21. Oveissi, F., Naficy, S., Lee, A., Winlaw, D. & Dehghani, F. Materials and manufacturing perspectives in engineering heart valves: a review. *Mater. Today Bio* **5**, 100038, DOI: <https://doi.org/10.1016/j.mtbio.2019.100038> (2020).
22. Wu, W. *et al.* A computational framework for atrioventricular valve modeling using open-source software. *J. Biomech. Eng.* **144**, 101012, DOI: <https://doi.org/10.1115/1.4054485> (2022).
23. Wu, W. *et al.* The effects of leaflet material properties on the simulated function of regurgitant mitral valves. *J. Mech. Behav. Biomed. Mater.* **142**, 105858, DOI: <https://doi.org/10.1016/j.jmbbm.2023.105858> (2023).
24. Zhang, W., Motiwale, S., Hsu, M.-C. & Sacks, M. S. Simulating the time evolving geometry, mechanical properties, and fibrous structure of bioprosthetic heart valve leaflets under cyclic loading. *J. Mech. Behav. Biomed. Mater.* **123**, 104745, DOI: <https://doi.org/10.1016/j.jmbbm.2021.104745> (2021).
25. Kong, F., Caballero, A., McKay, R. & Sun, W. Finite element analysis of mitraclip procedure on a patient-specific model with functional mitral regurgitation. *J. Biomech.* **104**, 109730, DOI: <https://doi.org/10.1016/j.jbiomech.2020.109730> (2020).
26. Bandyopadhyay, A. & Heer, B. Additive manufacturing of multi-material structures. *Mater. Sci. Eng. R: Reports* **129**, 1–16, DOI: <https://doi.org/10.1016/j.mser.2018.04.001> (2018).
27. Barroqueiro, B., Andrade-Campos, A., de Oliveira, J. D. & Valente, R. Design of mechanical heterogeneous specimens using topology optimization. *Int. J. Mech. Sci.* **181**, 105764, DOI: <https://doi.org/10.1016/j.ijmecsci.2020.105764> (2020).
28. Mazza, G. *et al.* Decellularized human liver as a natural 3D-scaffold for liver bioengineering and transplantation. *Sci. Reports* **5**, 13079, DOI: <https://doi.org/10.1038/srep13079> (2015).
29. Guyette, J. P. *et al.* Bioengineering human myocardium on native extracellular matrix. *Circ. Res.* **118**, 56–72, DOI: <https://doi.org/10.1161/CIRCRESAHA.115.306874> (2016).
30. Ohata, K. & Ott, H. C. Human-scale lung regeneration based on decellularized matrix scaffolds as a biologic platform. *Surg. Today* **50**, 633–643, DOI: <https://doi.org/10.1007/s00595-020-02000-y> (2020).
31. Li, G. *et al.* Bioinspired soft robots for deep-sea exploration. *Nat. Commun.* **14**, 7097, DOI: <https://doi.org/10.1038/s41467-023-42882-3> (2023).
32. Yang, X. *et al.* Bioinspired soft robots based on organic polymer-crystal hybrid materials with response to temperature and humidity. *Nat. Commun.* **14**, 2287, DOI: <https://doi.org/10.1038/s41467-023-37964-1> (2023).

33. Lim, C. *et al.* Tissue-like skin-device interface for wearable bioelectronics by using ultrasoft, mass-permeable, and low-impedance hydrogels. *Sci. Adv.* **7**, eabd3716, DOI: <https://doi.org/10.1126/sciadv.abd3716> (2021).
34. Kok, Y. *et al.* Anisotropy and heterogeneity of microstructure and mechanical properties in metal additive manufacturing: A critical review. *Mater. & Des.* **139**, 565–586, DOI: <https://doi.org/10.1016/j.matdes.2017.11.021> (2018).
35. Dufrêne, Y. F. *et al.* Imaging modes of atomic force microscopy for application in molecular and cell biology. *Nat. Nanotechnol.* **12**, 295–307, DOI: <https://doi.org/10.1038/nnano.2017.45> (2017).
36. Amo, C. A., Perrino, A. P., Payam, A. F. & Garcia, R. Mapping elastic properties of heterogeneous materials in liquid with angstrom-scale resolution. *ACS Nano* **11**, 8650–8659, DOI: <https://doi.org/10.1021/acsnano.7b04381> (2017). PMID: 28770996.
37. Rosalia, L., Hallou, A., Cochrane, L. & Savin, T. A magnetically actuated, optically sensed tensile testing method for mechanical characterization of soft biological tissues. *Sci. Adv.* **9**, eade2522, DOI: <https://doi.org/10.1126/sciadv.ade2522> (2023).
38. Guimarães, C. F., Gasperini, L., Marques, A. P. & Reis, R. L. The stiffness of living tissues and its implications for tissue engineering. *Nat. Rev. Mater.* **5**, 351–370, DOI: <https://doi.org/10.1038/s41578-019-0169-1> (2020).
39. Deplano, V. *et al.* Biaxial tensile tests of the porcine ascending aorta. *J. Biomech.* **49**, 2031–2037, DOI: <https://doi.org/10.1016/j.jbiomech.2016.05.005> (2016).
40. Quanjin, M., Rejab, M., Halim, Q., Merzuki, M. & Darus, M. Experimental investigation of the tensile test using digital image correlation (dic) method. *Mater. Today: Proc.* **27**, 757–763, DOI: <https://doi.org/10.1016/j.matpr.2019.12.072> (2020). First International conference on Advanced Lightweight Materials and Structures.
41. Laville, C., Pradille, C. & Tillier, Y. Mechanical characterization and identification of material parameters of porcine aortic valve leaflets. *J. Mech. Behav. Biomed. Mater.* **112**, 104036, DOI: <https://doi.org/10.1016/j.jmbbm.2020.104036> (2020).
42. Bruno, L., Decuzzi, P. & Gentile, F. Stress distribution retrieval in granular materials: A multi-scale model and digital image correlation measurements. *Opt. Lasers Eng.* **76**, 17–26, DOI: <https://doi.org/10.1016/j.optlaseng.2015.04.009> (2016). Special Issue: Optical Methods in Nanobiotechnology.
43. Salvati, E. & Korsunsky, A. An analysis of macro- and micro-scale residual stresses of Type I, II and III using FIB-DIC micro-ring-core milling and crystal plasticity FE modelling. *Int. J. Plast.* **98**, 123–138, DOI: <https://doi.org/10.1016/j.ijplas.2017.07.004> (2017).
44. Rokoš, O., Peerlings, R., Hoefnagels, J. & Geers, M. Integrated digital image correlation for micro-mechanical parameter identification in multiscale experiments. *Int. J. Solids Struct.* **267**, 112130, DOI: <https://doi.org/10.1016/j.ijsolstr.2023.112130> (2023).
45. You, H., Zhang, Q., Ross, C. J., Lee, C.-H. & Yu, Y. Learning deep implicit Fourier neural operators (IFNOs) with applications to heterogeneous material modeling with applications to heterogeneous material modeling. *Comput. Methods Appl. Mech. Eng.* **398**, 115296, DOI: <https://doi.org/10.1016/j.cma.2022.115296> (2022).
46. Mohammadzadeh, S. & Lejeune, E. Predicting mechanically driven full-field quantities of interest with deep learning-based metamodels. *Extrem. Mech. Lett.* **50**, 101566, DOI: <https://doi.org/10.1016/j.eml.2021.101566> (2022).

47. Kobeissi, H., Mohammadzadeh, S. & Lejeune, E. Enhancing mechanical metamodelling with a generative model-based augmented training dataset. *J. Biomech. Eng.* **144**, 121002, DOI: <https://doi.org/10.1115/1.4054898> (2022).
48. Hoq, E. *et al.* Data-driven methods for stress field predictions in random heterogeneous materials. *Eng. Appl. Artif. Intell.* **123**, 106267, DOI: <https://doi.org/10.1016/j.engappai.2023.106267> (2023).
49. Raissi, M., Perdikaris, P. & Karniadakis, G. Physics-informed neural networks: A deep learning framework for solving forward and inverse problems involving nonlinear partial differential equations. *J. Comput. Phys.* **378**, 686–707, DOI: <https://doi.org/10.1016/j.jcp.2018.10.045> (2019).
50. Karniadakis, G. E. *et al.* Physics-informed machine learning. *Nat. Rev. Phys.* **3**, 422–440 (2021).
51. Zhu, M., Zhang, H., Jiao, A., Karniadakis, G. E. & Lu, L. Reliable extrapolation of deep neural operators informed by physics or sparse observations. *Comput. Methods Appl. Mech. Eng.* **412**, 116064, DOI: <https://doi.org/10.1016/j.cma.2023.116064> (2023).
52. Yu, J., Lu, L., Meng, X. & Karniadakis, G. E. Gradient-enhanced physics-informed neural networks for forward and inverse PDE problems. *Comput. Methods Appl. Mech. Eng.* **393**, 114823, DOI: <https://doi.org/10.1016/j.cma.2022.114823> (2022).
53. Lu, L. *et al.* Physics-informed neural networks with hard constraints for inverse design. *SIAM J. on Sci. Comput.* **43**, B1105–B1132, DOI: <https://doi.org/10.1137/21M1397908> (2021).
54. Haghghat, E., Raissi, M., Moure, A., Gomez, H. & Juanes, R. A physics-informed deep learning framework for inversion and surrogate modeling in solid mechanics. *Comput. Methods Appl. Mech. Eng.* **379**, 113741, DOI: <https://doi.org/10.1016/j.cma.2021.113741> (2021).
55. Wu, W., Daneker, M., Jolley, M. A., Turner, K. T. & Lu, L. Effective data sampling strategies and boundary condition constraints of physics-informed neural networks for identifying material properties in solid mechanics. *Appl. Math. Mech.* **44**, 1039–1068, DOI: <https://doi.org/10.1007/s10483-023-2995-8> (2023).
56. Boddapati, J., Flaschel, M., Kumar, S., De Lorenzis, L. & Daraio, C. Single-test evaluation of directional elastic properties of anisotropic structured materials. *J. Mech. Phys. Solids* **181**, 105471, DOI: <https://doi.org/10.1016/j.jmps.2023.105471> (2023).
57. Rezaei, S., Harandi, A., Moeineddin, A., Xu, B.-X. & Reese, S. A mixed formulation for physics-informed neural networks as a potential solver for engineering problems in heterogeneous domains: Comparison with finite element method. *Comput. Methods Appl. Mech. Eng.* **401**, 115616, DOI: <https://doi.org/10.1016/j.cma.2022.115616> (2022).
58. Zhang, E., Dao, M., Karniadakis, G. E. & Suresh, S. Analyses of internal structures and defects in materials using physics-informed neural networks. *Sci. Adv.* **8**, eabk0644, DOI: <https://doi.org/10.1126/sciadv.abk0644> (2022).
59. Henkes, A., Wessels, H. & Mahnken, R. Physics informed neural networks for continuum micromechanics. *Comput. Methods Appl. Mech. Eng.* **393**, 114790, DOI: <https://doi.org/10.1016/j.cma.2022.114790> (2022).
60. Kamali, A., Sarabian, M. & Laksari, K. Elasticity imaging using physics-informed neural networks: Spatial discovery of elastic modulus and poisson's ratio. *Acta Biomater.* **155**, 400–409, DOI: <https://doi.org/10.1016/j.actbio.2022.11.024> (2023).
61. Chen, C. & Gu, G. Physics-informed deep-learning for elasticity: Forward, inverse, and mixed problems. *Adv. Sci.* **10**, DOI: <https://doi.org/10.1002/advs.202300439> (2023).

62. Wang, S., Wang, H. & Perdikaris, P. On the eigenvector bias of Fourier feature networks: From regression to solving multi-scale PDEs with physics-informed neural networks feature networks. *Comput. Methods Appl. Mech. Eng.* **384**, 113938, DOI: <https://doi.org/10.1016/j.cma.2021.113938> (2021).
63. Hao, Z. *et al.* PINNacle: A comprehensive benchmark of physics-informed neural networks for solving PDEs. *arXiv preprint arXiv:2306.08827* DOI: <https://doi.org/10.48550/arXiv.2306.08827> (2023).
64. Rathore, P., Lei, W., Frangella, Z., Lu, L. & Udell, M. Challenges in training PINNs: A loss landscape perspective. *arXiv preprint arXiv:2402.01868* DOI: <https://doi.org/10.48550/arXiv.2402.01868> (2024).
65. Song, C. & Wang, Y. Simulating seismic multifrequency wavefields with the Fourier feature physics-informed neural network. *Geophys. J. Int.* **232**, 1503–1514, DOI: <https://doi.org/10.1093/gji/ggac399> (2022).
66. Quincy A. Huhn, M. E. T. & Ragusa, J. C. Physics-informed neural network with Fourier features for radiation transport in heterogeneous media. *Nucl. Sci. Eng.* **197**, 2484–2497, DOI: <https://doi.org/10.1080/00295639.2023.2184194> (2023).
67. Yazdani, A., Lu, L., Raissi, M. & Karniadakis, G. E. Systems biology informed deep learning for inferring parameters and hidden dynamics. *PLoS Comput. Biol.* **16**, e1007575, DOI: <https://doi.org/10.1371/journal.pcbi.1007575> (2020).
68. Daneker, M., Zhang, Z., Karniadakis, G. E. & Lu, L. *Systems Biology: Identifiability Analysis and Parameter Identification via Systems-Biology-Informed Neural Networks*, 87–105 (Springer US, New York, NY, 2023).
69. Myers, K. & Ateshian, G. A. Interstitial growth and remodeling of biological tissues: Tissue composition as state variables. *J. Mech. Behav. Biomed. Mater.* **29**, 544–556, DOI: <https://doi.org/10.1016/j.jmbbm.2013.03.003> (2014).
70. Oomen, P. J. A., Holland, M. A., Bouten, C. V. C., Kuhl, E. & Loerakker, S. Growth and remodeling play opposing roles during postnatal human heart valve development. *Sci. Reports* **8**, 1235, DOI: <https://doi.org/10.1038/s41598-018-19777-1> (2018).
71. Fruleux, A. & Boudaoud, A. Modulation of tissue growth heterogeneity by responses to mechanical stress. *Proc Natl Acad Sci U S A* **116**, 1940–1945, DOI: <https://doi.org/10.1073/pnas.1815342116> (2019).
72. Hormuth, D. A. *et al.* Mechanism-based modeling of tumor growth and treatment response constrained by multiparametric imaging data. *JCO Clin. Cancer Informatics* 1–10, DOI: <https://doi.org/10.1200/CCI.18.00055> (2019).
73. Song, Y., Schiffer, A. & Tagarielli, V. L. The effects of heterogeneous mechanical properties on the response of a ductile material. *Sci. Reports* **11**, 18170, DOI: <https://doi.org/10.1038/s41598-021-97495-x> (2021).
74. Jiang, J., Chen, Z., Ma, H., Xing, H. & Li, X. Strength-ductility synergy in heterogeneous-structured metals and alloys. *Matter* **5**, 2430–2433, DOI: <https://doi.org/10.1016/j.matt.2022.05.023> (2022).
75. Molladavoodi, S., Gorbet, M., Medley, J. & Ju Kwon, H. Investigation of microstructure, mechanical properties and cellular viability of poly(L-lactic acid) tissue engineering scaffolds prepared by different

- thermally induced phase separation protocols. *J. Mech. Behav. Biomed. Mater.* **17**, 186–197, DOI: <https://doi.org/10.1016/j.jmbbm.2012.08.021> (2013).
76. Budday, S. *et al.* Towards microstructure-informed material models for human brain tissue. *Acta Biomater.* **104**, 53–65, DOI: <https://doi.org/10.1016/j.actbio.2019.12.030> (2020).
  77. Zhang, C., Liu, C. & Zhao, H. Mechanical properties of brain tissue based on microstructure. *J. Mech. Behav. Biomed. Mater.* **126**, 104924, DOI: <https://doi.org/10.1016/j.jmbbm.2021.104924> (2022).
  78. Moore, D. & Russell, S. J. Gaussian process random fields. In Cortes, C., Lawrence, N., Lee, D., Sugiyama, M. & Garnett, R. (eds.) *Advances in Neural Information Processing Systems*, vol. 28 (Curran Associates, Inc., 2015).
  79. Koos, K., Molnár, J., Kelemen, L., Tamás, G. & Horvath, P. DIC image reconstruction using an energy minimization framework to visualize optical path length distribution. *Sci. Reports* **6**, 30420, DOI: <https://doi.org/10.1038/srep30420> (2016).
  80. Weinberg, E. J. & Kaazempur-Mofrad, M. R. On the constitutive models for heart valve leaflet mechanics. *Cardiovasc. Eng.* **5**, 37–43, DOI: <https://doi.org/10.1007/s10558-005-3072-x> (2005).
  81. Larkin, K. G. Reflections on shannon information: In search of a natural information-entropy for images. *arXiv preprint arXiv:1609.01117* DOI: <https://doi.org/10.48550/arXiv.1609.01117> (2016).
  82. Khan, T. M., Naqvi, S. S. & Meijering, E. Leveraging image complexity in macro-level neural network design for medical image segmentation. *Sci. Reports* **12**, 22286, DOI: <https://doi.org/10.1038/s41598-022-26482-7> (2022).
  83. Logg, A. & Wells, G. N. DOLFIN: Automated finite element computing. *ACM Trans. Math. Softw.* **37**, DOI: <https://doi.org/10.1145/1731022.1731030> (2010).
  84. Ryu JeongAh, J. W. K. Current status of musculoskeletal application of shear wave elastography. *Ultrasonography* **36**, 185–197, DOI: <https://doi.org/10.14366/usg.16053> (2017).
  85. Lu, L., Meng, X., Mao, Z. & Karniadakis, G. E. DeepXDE: A deep learning library for solving differential equations. *SIAM Rev.* **63** (2021).
  86. Wu, C., Zhu, M., Tan, Q., Kartha, Y. & Lu, L. A comprehensive study of non-adaptive and residual-based adaptive sampling for physics-informed neural networks. *Comput. Methods Appl. Mech. Eng.* **403**, 115671, DOI: <https://doi.org/10.1016/j.cma.2022.115671> (2023).
  87. Liu, D. C. & Nocedal, J. On the limited memory BFGS method for large scale optimization. *Math. Program.* **45**, 503–528, DOI: <https://doi.org/10.1007/BF01589116> (1989).
  88. Hayford, J., Goldman-Wetzler, J., Wang, E. & Lu, L. Speeding up and reducing memory usage for scientific machine learning via mixed precision. *arXiv preprint arXiv:2401.16645* DOI: <https://doi.org/10.48550/arXiv.2401.16645> (2024).
  89. Bonet, J. & Wood, R. D. *Nonlinear Continuum Mechanics for Finite Element Analysis* (Cambridge University Press, 2008), 2 edn.